

Oxygen Ion Energization at Mars: Comparison of MAVEN and Mars Express Observations to Global Hybrid Simulation

R. Jarvinen^{1, 6}, D.A. Brain², R. Modolo³, A. Fedorov⁴, M. Holmström⁵

R. Jarvinen, riku.jarvinen@fmi.fi

¹Finnish Meteorological Institute,
Helsinki, Finland

²University of Colorado at Boulder,
Laboratory for Atmospheric and Space
Physics, Boulder, CO, United States

³Laboratoire Atmospheres, Milieux,
Observations Spatiales, Paris, France

⁴IRAP, Toulouse, France

⁵IRF Swedish Institute of Space Physics
Kiruna, Kiruna, Sweden

⁶Department of Electronics and
Nanoengineering, School of Electrical

This article has been accepted for publication and undergone full peer review but has not been through the copyediting, typesetting, pagination and proofreading process, which may lead to differences between this version and the Version of Record. Please cite this article as doi: 10.1002/2017JA024884

Abstract. We study oxygen ion energization in the Mars-solar wind interaction by comparing particle and magnetic field observations on the MAVEN and Mars Express missions to a global hybrid simulation. We find that large-scale structures of the Martian induced magnetosphere and plasma environment as well as the Mars heavy ion plume as seen by multi-spacecraft observations are reproduced by the model. Using the simulation we estimate the dynamics of escaping oxygen ions by analyzing their distance and time of flight as a function of the gained kinetic energy along spacecraft trajectories. In the upstream region the heavy ion energization resembles single particle solar wind ion pickup acceleration as expected, while within the induced magnetosphere the energization displays other features including the heavy ion plume from the ionosphere. Oxygen ions take up to 80 s and travel the distance of 20 000 km after their emission from the ionosphere to the induced magnetosphere or photoionization from the neutral exosphere before they have reached energies of 10 keV in the plume along the analyzed spacecraft orbits. Lower oxygen ion energies of 100 eV are reached faster in 10-20 s over the distance of 100-200 km in the plume. Our finding suggests that oxygen ions are typically observed within the first half of their gyro phase

Engineering, Aalto University, Espoo,
Finland

if the spacecraft periapsis is on the hemisphere where the solar wind convection electric field points away from Mars.

Keypoints:

- Multi-spacecraft observations of the Mars heavy ion plume
- Estimation of ion time and distance of flight based on a global model
- Oxygen ions observed near Mars within the first half of their gyro phase

Accepted Article

1. Introduction

Mars is the second smallest object in the solar system with a significant atmosphere. The planet has likely lost a lot, even an oceanful, of water since its childhood. As 89% of the mass of the water molecule is in oxygen, most of the energy and momentum required to remove constituents of water from a gravity well of a celestial body goes to oxygen. It is debated how much oxygen and other heavy elements the solar wind has eroded from Mars during the age of the solar system.

The solar wind drives the erosion of ionized volatiles from globally unmagnetized Mars and Venus through their atmospheres via several channels [Lundin, 2011]. The largest observed structure of the ion escape from Mars was recently termed as the heavy ion plume [Brain *et al.*, 2010]. The plume forms when the solar wind convection electric field accelerates heavy ions of atmospheric origin from ionospheric altitudes to several planetary radii distances. These planetary pickup ions follow cycloid trajectories with the Larmor radii large or comparable to the size of an induced magnetosphere in the magnetized solar wind plasma flow.

The Mars induced magnetosphere and ion escape are hemispherically asymmetric as seen in *in situ* observations, for example, on the Mars Express (MEX) mission [Fedorov *et al.*, 2006; Barabash *et al.*, 2007] and on the Mars Atmosphere and Volatile Evolution (MAVEN) mission [Dong *et al.*, 2015; Jakosky *et al.*, 2015] as well as in global simulations of the Mars-solar wind interaction [Brecht, 1990; Kallio *et al.*, 2010; Najib *et al.*, 2011; Ma *et al.*, 2015; Modolo *et al.*, 2016; Ledvina *et al.*, 2017]. Typically the near space around Mars is divided in four quadrants or hemispheres to analyze asymmetries of the

ion escape [Nilsson *et al.*, 2011; Brain *et al.*, 2015]. The plume is located in the hemisphere where the solar wind convection electric field points away from the planet, termed the $+E_{\text{SW}}$ hemisphere, which dominates the ion escape rate compared to the opposite ($-E_{\text{SW}}$) hemisphere. The orientation of the plume perpendicular to the Mars-sun axis is along the solar wind convection electric field. The distance heavy ions reach along the electric field is determined by their Larmor radii and, thus, by the magnitude of the interplanetary magnetic field (IMF) [Curry *et al.*, 2015a; Jarvinen *et al.*, 2016]. The longer the distance, the higher the bulk energy over a Larmor period [Jarvinen and Kallio, 2014]. Further, the heavy ion plume merges continuously to the tailward escape channels when moving from the Mars magnetosheath towards the wake [Dong *et al.*, 2015]. We refer to the wake or the tail as the general region inside the induced magnetosphere boundary (IMB) where no solar wind ions are observed. In addition to the IMB several boundaries have been defined between the wake and the magnetosheath, which is the region where the shocked solar wind flows downstream of the bow shock. These include, the magnetic pileup boundary, the ion composition boundary, the protonopause, the planetopause and the solar wind dropout boundary [see, e.g., Kallio, 2001; Barabash *et al.*, 2007; Matsunaga *et al.*, 2017, and references therein].

In this work we analyze the formation of the Mars heavy ion plume as seen by multi-spacecraft observations and a self-consistent global hybrid simulation. In the analysis we concentrate on energization of atomic and molecular oxygen ions. We choose for analysis spacecraft orbits on the MEX and MAVEN missions with periapses two hours apart from each other displaying a detection of the large-scale heavy ion plume. In the analysis we concentrate on comparing ion spectral and magnetic field observations

between the spacecraft *in situ* instrument measurements and a virtual spacecraft in the global hybrid model. Further, we use the model to analyze finite Larmor radius (FLR) effects of planetary oxygen ions. We estimate the kinetic energies of the planetary ions as a function of distance of flight and time of flight after photoionization from the neutral exosphere or emission from the ionosphere toward the induced magnetosphere.

The following coordinate systems are used in this work. Spacecraft observations are presented in the Mars-Solar Orbital (MSO) coordinates, where the x -axis points towards the Sun from the center of the planet, the y -axis is anti-parallel to the orbital velocity vector of Mars around the Sun and the z -axis completes the right-handed coordinate system. In the model the coordinate system is similar to the MSO system with the exception that the x -axis points towards the solar wind flow instead of the Sun. That is, the aberration of the incident solar wind velocity vector of few degrees in the rest frame of Mars caused by the planetary orbital motion is neglected in the model. The radius of Mars ($R_M = 3390$ km) is used as the unit of length in the figures.

The article is organized as follows. In the next section we briefly describe the used *in situ* ion spectrometer and magnetic field observations on the MEX and MAVEN missions. Then we present the RHybrid global hybrid simulation code. In the results section we present results from our numerical modeling experiment and compare them to the observations. At the end we discuss and summarize our findings.

2. Spacecraft observations

An orbit from MAVEN and an orbit from MEX on Jan 25, 2015 were chosen for analysis as ion spectrometers on both spacecraft showed a clear detection of the heavy ion plume on that day (Figure 3 panels c and g). The spacecraft orbit geometries are shown in Figure

1. MEX is close to the noon-midnight orbit configuration whereas MAVEN's trajectory is between the terminator and noon-midnight planes. Observational data from several instruments on the MAVEN and MEX mission are analyzed here.

The Analyzer of Space Plasma and Energetic Atoms (ASPERA-3) particle package on MEX (Mars orbit insertion in 2003) includes the Ion Mass Analyzer (IMA) mass-resolving ion spectrometer [Barabash and Lundin, 2006]. ASPERA-3/IMA measures ions in the energy range from 10 eV/ e to 36 keV/ e , where e is the positive elementary charge, with the nominal time resolution of 196 s. Suprathermal and Thermal Ion Composition (STATIC) [McFadden *et al.*, 2015] and Solar Wind Ion Analyzer (SWIA) [Halekas *et al.*, 2015] ion spectrometers on MAVEN (Mars orbit insertion in 2014) have both intrinsic cadence of 4 s. STATIC is a mass-resolving instrument with the energy range from 0.1 eV/ e to 30 keV/ e , whereas SWIA measures all ions without mass separation capability in the energy range from 5 eV/ e to 25 keV/ e . Thus, MAVEN's modern ion spectrometers are able to measure ions at lower energies and higher time resolution than the ion spectrometer on MEX. MAVEN's magnetometer uses tri-axial fluxgate sensors operating at an intrinsic sampling rate of 32 vector measurements per second, while MEX does not have a magnetometer.

Figure 2 displays the magnetic field observed by MAVEN's magnetometer [Connerney *et al.*, 2015]. MVN/SWIA, MVN/STATIC and MEX/ASPERA-3/IMA observations are plotted in Figure 3. Structures of the Martian induced magnetosphere are evident in magnetic and particle observations and they are described in the Results section.

3. Global hybrid code: RHybrid

We use a highly parallel C++ global hybrid simulation platform for planetary plasma interactions named RHybrid, which was recently developed at the Finnish Meteorological

Insitute (FMI) [Jarvinen and Sandroos, 2013]. In the code ions are modeled as grid cell sized and shaped macroscopic particle clouds (macroparticles or macroions) moving under the Lorentz force. Tri-linear macroparticle weighting is applied when ion moments are estimated in the Cartesian simulation mesh of cubic grid cells. Grid cells and particles are distributed to computing cores via the Message Passing Interface (MPI) based on the FMI's ParGrid and Corsair high-performance computing (HPC) simulation libraries [Hietala et al., 2012; Sandroos, 2013]. Computational load is dynamically balanced between the MPI processing elements during a simulation run by the Zoltan library using the Recursive Coordinate Bisection algorithm [Boman et al., 2012]. In this work the RHybrid code was run on 720 computing cores of the FMI's Cray XC30 system for about 16k core hours per simulation run.

In the simulation runs analyzed here the magnetic field (\vec{B}) is stored on grid cell faces and the electric field (\vec{E}) is estimated on grid cell nodes and edges. This Yee type staggered grid guarantees divergence-free propagation of magnetic field according to Faraday's law [Dai and Woodward, 1998]. Electrons are treated as a massless and pressureless fluid, which provides quasi-neutrality of the plasma. Thus, the electron dynamics are governed by the equations $q_e n_e \vec{U}_e = \vec{J} - \sum_i q_i n_i \vec{V}_i$ and $q_e n_e = \sum_i q_i n_i$, where q_e , n_e and \vec{U}_e are the electron charge, number density and velocity, q_i , n_i and \vec{V}_i are the ion charge, number density and velocity with the summation i over all macroions in a grid cell and \vec{J} is the total current density defined by Ampere's law. Thus, the summed electron ($q_e n_e \vec{U}_e$) and ion ($\sum_i q_i n_i \vec{V}_i$) current densities in a grid cell are equal to the total current density while the total charge density in a grid cell remains zero.

The magnetic field is propagated by Faraday's law $\partial\vec{B}/\partial t = -\nabla \times \vec{E}$, where the Ohm's law reads $\vec{E} = -\vec{U}_e \times \vec{B} + \eta\vec{J}$ and η is a given explicit resistivity profile. The resistivity is used to add diffusion in the propagation of the magnetic field to increase numerical stability, while the resistive electric field term is not included explicitly in the Lorentz force. The magnetic diffusion time scale determined by the induction equation is $\tau_d = \mu_0 L_B^2 / \eta$, where μ_0 is the permeability of free space and L_B is the scale length of the magnetic field [e.g. *Koskinen, 2011*]. The value of η above the inner boundary is set as $\eta = 0.02\mu_0\Delta x^2/\Delta t$, where Δx is a grid cell side length and Δt is the time step (see Table 1). By setting $L_B = \Delta x$, which is the smallest possible scale length of the magnetic field in a simulation, the lower limit of the magnetic diffusion time comes $\tau_d = \Delta t/0.02 = 50\Delta t$. That is, η allows the diffusion of the magnetic field only on time scales much longer than the simulation time step.

In the analyzed runs the ionospheric obstacle to the solar wind flow is modeled as a superconducting sphere by setting the resistivity as zero at and inside the inner boundary. Thus, τ_d becomes infinite and the magnetic field does not diffuse through the obstacle. Further, ions impacting the inner boundary are absorbed and removed from the simulation and the electron velocity is set as zero inside the inner boundary.

The simulation domain is surrounded by a layer of passive cells called ghost cells, where boundary conditions are enforced. The solar wind is implemented at the front wall by injecting moving Maxwellian populations of H^+ and He^{++} ions. The perpendicular component of the IMF to the plasma flow is held constant in the ghost cells of the front wall and, thus, convects in the domain with the solar wind. The flow-aligned component of the IMF is implemented as an initial magnetic field derived from potential flow, which has

zero radial component at the inner boundary and is homogeneous at infinity [*Shimazu, 1999; Kallio et al., 2006*]. This field corresponds to a laminar flow around a sphere.

Planetary ions are injected in the simulation from the inner boundary (Mars ionospheric emission) and via photoionization of the Mars exosphere. Both atomic (O^+) and molecular (O_2^+) oxygen ions are emitted from the ionosphere and H^+ and O^+ photoions are created from the exosphere. The ionospheric emission has a maximum flux at noon and $\cos(SZA)$, where SZA is the solar-zenith angle, dependence towards terminator where the flux reaches 10% of the noon value and is constant for the nightside. The exospheric photoionization rate is constant above the inner boundary except in the shadow of the planet where no photoions are created. Oxygen and hydrogen neutral corona profiles are taken from the "Run C (solar maximum with exosphere)" input definitions of the "Intercomparison of Global Models and Measurements of the Martian Plasma Environment" International Space Science Institute (ISSI) Team's second meeting [*Modolo et al., 2016*]. The total ionospheric emission rates were chosen so that they best fit the spacecraft orbits analyzed here [see, e.g., *Jarvinen et al., 2009*]. This meant that the ionospheric emission rates were increased by a factor of 3 for this study compared to the ionospheric emission in an earlier run where solar minimum exospheric photoionization conditions from ISSI team's first meeting were used [*Kallio et al., 2010*].

Kallio and Janhunen [2003] describe details of the used numerical algorithm with the following exceptions. In RHybrid the electron velocity is determined directly at grid cell nodes, which means no cell volume average to node interpolation is needed. The electric current density is evaluated at the edges of the grid cell faces instead of the grid cell nodes [*Pohjola and Kallio, 2010*]. Further, no artificial macroparticle splitting and joining nor

adaptive mesh refinements are used in RHybrid. The number of particles and grid cells can be much higher in parallelized than sequential simulation codes.

Table 1 lists the most important simulation parameters and upstream conditions of the RHybrid simulation runs analyzed in this work. Run 1 describes the MAVEN inbound upstream conditions and Run 2 describes the MAVEN outbound and MEX inbound upstream conditions for the analyzed orbit case. The simulation was run until the Martian induced magnetosphere and plasma environment were formed and the simulation had reached near stationary development after initial transients.

4. Results

Figures 1d-f (lower panels) display the number density and bulk velocity of oxygen ions in the simulation Run 2. Photoions originating from the exosphere are seen away from near vicinity of the planet as a spherically symmetric distribution (light blue and green colors), while in the night side and close to the planet the dense plasma sheet and the heavy ion plume of ionospheric origin are evident (red color). The plasma sheet and the plume are oriented along the electric field shown as white arrows in Figure 1e. Regions of highest oxygen flux (blue-red velocity vectors in Figure 1f) include mostly the plume, the plasma sheet and the magnetosheath on the $+E_{SW}$ hemisphere. The velocity increases in concert with increasing distance along the electric field both in the day side and in the night side outside of the wake. The plume sampled by MAVEN (indicated by yellow arrows on blue spacecraft trajectory) crosses some of these high flux regions in the model, whereas the plume sampled by MEX (indicated by yellow arrows on red spacecraft trajectory) are mostly not in the high flux regions in the model.

4.1. Magnetic field

Figure 2 compares the magnetic field observed by MAVEN with both simulation runs. Run 1 (inbound upstream conditions) is plotted until periapsis and Run 2 (outbound upstream conditions) from periapsis. Crossing of the quasi-perpendicular region of the bow shock are seen as abrupt jumps in the magnetic field at 12:30 (BS in) and 14:15 (BS out) both in the observations and in the model. The periapsis occurs at 13:20 (Peri) and the field has a local minimum and a temporary sign change in all components when the spacecraft is in the ionosphere. In the model the magnitude of the magnetic field decreases already for a few minutes before and after the periapsis when the orbit is inside the inner boundary of the model (13:12 - 13:27). The central tail current sheet is crossed at 13:40 (CS) when the field magnitude has a local minimum and the B_x and B_z components change sign both in the observations and in the model.

4.2. Ion spectra

Figure 3 compares observed and modeled ion time-energy spectrograms of heavy and light ions along trajectories of both spacecraft. In the top two rows the upstream beams of the solar wind H^+ and He^{++} ions and the planetary environment with the shocked solar wind plasma are evident. Heating of the upstream solar wind ion beams occurs at the bow shock. Near the periapsis the solar wind dropout boundaries occur at 13:00 and 13:30 UT along the MAVEN trajectory and at 14:30 and 15:40 along the MEX trajectory both in the model and in the observations. The wake region is mostly void of light ions. Exospheric H^+ photoions are seen in the model spectra as light blue color scattered counts. Further, the modeled light ion composition is dominated by the solar wind H^+ with a minor He^{++}

component except near the periapsis where the composition is dominated by sporadic exospheric H^+ ion counts in the wake (green color in Figures 3b and 3f).

In the bottom two rows of Figure 3 heavy ions are analyzed. Lowest energies ($\lesssim 10$ eV) occur in and near the ionosphere (periapsis) in the observations and in the model.

Exospheric O^+ photoions are seen in the model as light blue color scattered counts throughout the spectra. After the periapsis crossing the heavy ion plume is seen as increasing energies from 10 eV up to several keVs (MAVEN: 13:20 - 13:50 UT and MEX: 15:30 - 15:50 UT). In the simulation the heavy ion composition near the periapsis and the plume is dominated by the O^+ and O_2^+ ions of ionospheric origin. The exospheric O^+ photoions dominate the composition elsewhere.

4.3. Distance and Time of Flight analysis

Figure 4 analyses the oxygen ion energization in the simulation Run 2 along the spacecraft trajectories using 2-dimensional histograms of distance of flight (DoF) and time of flight (ToF) versus particle energy. The orbits of both spacecraft are divided in four parts for detailed analysis of the ion dynamics in different plasma regions around Mars as shown in Figure 3 (columns from left): inbound upstream (first column), periapsis/ionosphere (second column), plume (third column) and outbound upstream (fourth column).

The DoF and ToF energy histograms were created as follows. Macroparticles in every grid cell touching the spacecraft orbits were recorded until 25×10^6 macroions were reached per orbit. This took about 147 time steps (1.1 seconds) with about 500 cells per orbit within the simulation domain. Each macroparticle carried the following extra information for the analysis: simulation time, particle coordinates and velocity at its injection (or ionization) in the simulation. Together with simulation time, particle coordinates and

velocity at its observation (or collection) and the statistical weight of the particle the histograms were constructed. The DoF (Δd) was determined as the straight distance between the observation point and the injection point of a particle. Similarly, the ToF (Δt) was determined as the duration between the observation time and the injection time of a particle. The particle energy (E) was determined from its velocity at the collection. Injection velocities were generally very low compared to the velocities at observation, which means that the particle energy in Figure 4 is almost the same as the energy gained by the particle since its injection in the simulation ($E_{\text{observation}} \approx \Delta E = E_{\text{observation}} - E_{\text{injection}}$).

Figure 4 reveals several details about oxygen ion energization in the simulation. The ion energy as a function of the distance of flight in the top row (MAVEN) and the third row (MEX) show that the more distance the particle has to its ionization point when collected in a grid cell on the spacecraft orbit, the higher the particle energy in general. The same is true for the time of flight (second row / MAVEN and bottom row / MEX): the more time the particle has spent in the simulation when collected, the higher the energy in general. The correlation is almost \sim linear in log-log scale especially in the upstream solar wind regions (first and fourth columns). In the upstream region the oxygen ion composition is purely exospheric O^+ as seen in panels d and h of Figure 3.

Also more complicated dependencies between the DoF and the ToF and the ion energy occur in the simulation. The histograms display non-linearity in the log-log scale mostly near the planet for both spacecraft orbits. A strong source of oxygen ions emitted from the ionosphere is seen as red regimes along both orbits in the periapsis and plume columns of Figure 4, while the light blue, green and yellow regimes are mostly exospheric oxygen

photoions (separate figures for ionospheric and exospheric populations not shown). The oxygen ions emitted from the ionosphere in the periapsis column of both spacecraft are at lower energies than in the plume column as expected. In the MAVEN periapsis column the red ionospheric population has energies of about 10-50 eV and DoF of 1000-2000 km (Figure 4b) and ToF of 100-300 s (Figure 4f). In the MEX periapsis column the red ionospheric population has a broader spread in energy of \approx 10-200 eV likely due the higher periapsis altitude of MEX than MAVEN allowing higher energies. The ionospheric population in the MEX periapsis has DoF of 1000-10000 km (Figure 4j) and ToF of 100-400 s (Figure 4n).

In the plume column of both spacecraft the red ionospheric population has moved to higher energies and displays more linear or monotonously increasing features as a function of DoF and ToF than in the periapsis column. Along the MEX orbit the ionospheric plume overlaps with the exospheric photoions above 1 keV (Figures 4k and Figure 4o). Along the MAVEN orbit the ionospheric plume is seen at somewhat lower energies than the exospheric photoions (Figures 4c and Figure 4g). Low energy ionospheric oxygen at 10 eV and DoF = 100 km and ToF = 10-20 s are seen in the MEX plume column (Figures 4k and Figure 4o). These can be associated with the ionospheric emission from the low altitude night side wake region where the acceleration of heavy ions is less efficient than higher up and away from the wake.

5. Discussion

MAVEN and MEX observations at Mars on Jan 25, 2015 show the heavy ion plume signature in the $+E_{SW}$ hemisphere. In the model the ionospheric heavy ion plume is also evident along the trajectories of both spacecraft. MEX sampled the plume near the

noon-midnight orbit configuration whereas MAVEN sampled the plume along the orbit between the terminator plane and the noon-midnight plane. The plume observations were about two hours apart from each other between MAVEN and MEX. This indicates that the plume is a stable structure over temporal scale of at least few hours provided that the orientation of the large scale solar wind convection electric field remains stable. This is in agreement with single spacecraft studies and models [*Dubinin et al.*, 2008; ?; *Dong et al.*, 2015; *Curry et al.*, 2015b; *Jarvinen et al.*, 2016].

In the simulation the energization of oxygen ions starts at energies of $\lesssim 10$ eV and reaches several keVs in the Mars induced magnetosphere along the spacecraft trajectories. In the upstream solar wind region, where the pure ion pickup is the large scale acceleration process, the correlation of distance and time of flight (DoF/ToF) with the oxygen ion energy is linear on a log-log scale according to the model. The linearity goes up to ~ 20 000 km and ~ 30 s when oxygen ions have reached the energy of 10 keV along these spacecraft trajectories. Also other parts of the orbits display monotonously increasing structures in the oxygen energies as a function of DoF and ToF. This implies that oxygen ions are within the first half of their gyro phase after ionization from the exosphere or emission from the ionosphere. Escaping oxygen ions have not had time to get accelerated to higher gyro phases as the periapses of the spacecraft orbits analyzed here are on the $+E_{SW}$ hemisphere. Higher oxygen ion energies and gyro phases would be observed during orbits with the apoapsis on the $+E_{SW}$ hemisphere. All in all, oxygen ions display strong FLR behaviour in their energization.

Let us consider the FLR effects and the mass-to-charge ratio of the planetary ion species in light of our DoF and ToF analysis. The Larmor period and radius of a charged particle

are $\tau_L = 2\pi m/(qB)$ and $r_L = mV_{\perp}/(qB)$, respectively, where m and q are the mass and electric charge of the particle and V_{\perp} is the velocity of the particle perpendicular to the magnetic field. The ratio for atomic oxygen ions is 16 times the ratio of the protons. Thus, protons should undergo 16 gyrations in the same time when atomic oxygen ions undergo one, provided that electric and magnetic field are the same and particles start at rest. Also, H^+ have the Larmor radius of 1/16 times the Larmor radius of O^+ . The gyro motion of planetary pickup protons along the space should maybe be more pronounced than the gyro motion of oxygen, which only displays less than about the first half of the first gyro phase of oxygen pickup ions as discussed in the previous paragraph.

Figure 5 shows the DoF and ToF versus particle energy histograms of the exospheric hydrogen photoions becoming picked up by the upstream solar wind flow along the MAVEN trajectory in the inbound upstream region. These can be compared to panels a and e of Figure 4 for oxygen ions. The motion over several gyro periods can be seen for planetary protons. All proton gyro phases are evident in the plot as kinetic energies are not monotonously related to DoF nor ToF. The gyro motion of the pickup protons occurs at spatial and temporal scales small enough that gyro phases of their multiple gyrations around the magnetic field are seen along the analyzed spacecraft orbits around Mars. This can be estimated as follows.

Let us consider the pickup ion (PUI) dynamics in the single particle picture in homogeneous electric and magnetic fields [e.g. *Jarvinen and Kallio, 2014*] corresponding to upstream conditions of Run 2 (see numerical values of the parameters in Table 1). An O^+ ion picked up from rest (O_{PUI}^+) by the undisturbed solar wind has a gyro radius and period of $r_L(O_{PUI}^+) = m_{O^+}V_{E \times B}/(eB) = 5720$ km and $\tau_L(O_{PUI}^+) = 2\pi m_{O^+}/(eB) = 155$

s, where m_{O^+} is the oxygen mass, the drift velocity reads $V_{E \times B} = \vec{E} \times \vec{B} / B^2$ and $\vec{E} = -\vec{V} \times \vec{B}$. At the middle of the gyro phase the particle reaches the maximum energy of $E_{\text{kin}}^{\text{max}}(\text{O}_{\text{PUI}}^+) = 4(0.5m_{\text{O}^+}V_{E \times B}^2) = 18 \text{ keV}$ after $\tau_{\text{L}}(\text{O}_{\text{PUI}}^+)/2 = 78 \text{ s}$ from ionization and after moving $d_{\text{L}}(\text{O}_{\text{PUI}}^+)/2 = 22890 \text{ km}$ along its cycloid trajectory, where $d_{\text{L}}(\text{O}_{\text{PUI}}^+) = 8r_{\text{L}}(\text{O}_{\text{PUI}}^+)$ is the length of one full gyro cycloid. For $\text{O}_{2,\text{PUI}}^+$ multiply these values by two and for H_{PUI}^+ divide by 16.

How do these spatial scales compare with the spacecraft orbits? MAVEN detected the plume below the altitude of $\sim 3000 \text{ km}$ and MEX below the altitude of $\sim 2000 \text{ km}$ along the analyzed orbits. The apoapses of the orbits are 6400 km for MAVEN and 10500 km for MEX. Thus, O^+ and O_2^+ ions moving in the undisturbed upstream solar wind would require much longer distances than the MAVEN and MEX apoapses to complete their first half of the gyro period. However, protons can undergo several gyrations within these altitude ranges.

In principle the spacecraft could detect planetward oxygen ions at $2000\text{-}3000 \text{ km}$ altitudes that have been ionized higher up in the exosphere and would have already completed the first half or even several gyro periods. These would be planetary ions moving from the $-E_{\text{SW}}$ hemisphere towards the $+E_{\text{SW}}$ hemisphere and some of them would precipitate in the ionosphere ("the planetward heavy ion plume") [Luhmann *et al.*, 1992; Hara *et al.*, 2013; Curry *et al.*, 2015b; Leblanc *et al.*, 2015]. However, the density of this population would be very low compared to the ionospheric source forming the heavy ion plume on the $+E_{\text{SW}}$ hemisphere.

According to the model the strongest oxygen ion flux in the plume is seen with ions that have travelled $\text{DoF} = 200\text{-}3000 \text{ km}$ in time of $\text{ToF} = 20\text{-}80 \text{ s}$ after ionization, and

have reached the energies of about 100 eV - 1 keV. In the periapsis column of Figure 4 intense populations of low energy (10-100 eV) oxygen ions with long flight times (ToF ≥ 100 s) and distances (DoF = 1000-10000 km) are seen. These populations appear to be non-monotonous with respect to energy and ToF and DoF or at least have less efficient acceleration compared to pure ion pickup in the upstream. Long life times at low energies are consistent with high planetary ion densities at low altitudes, which can lead to shielding from the large scale convection electric field of the solar wind [e.g. *Jarvinen et al.*, 2009]. More efficient acceleration of heavy ions occurs when particles from this seed population emitted from the ionosphere reach higher altitudes in the induced magnetosphere as seen in the plume column of Figure 4.

5.1. Limitations

The following limitations should be noted. All ions of each species are collected from grid cells of the model that touch the spacecraft orbits. That is, no instrument geometrical factors or field of view effects are considered but the analyzed model spectra are omnidirectional. Including the observational factors would remove some of the ion counts in Figures 3 - 5. Further, the MAVEN orbit passes inside the inner boundary of the model between 13:12 - 13:27 UT, which is seen as a minimum in the magnitude of the magnetic field in Figure 2d. No Mars magnetic crustal anomalies are included in the analyzed simulations runs.

The DoF and ToF measure the time and distance from an ionization point to an observation point as a function of particle energy. For the ionospheric populations "the ionization" corresponds to the emission of an ion from the ionosphere toward the induced magnetosphere as implemented at the inner boundary of the model. In reality most of

the ionospheric ions may have been ionized deep in the ionosphere before their departure (emission) toward the induced magnetosphere. Thus, the modeled DoF and ToF should be interpreted as lower limits for the ionospheric populations. For the exospheric populations this is not an issue as their ionization occurs above the inner boundary of the simulation.

In this work finite resistivity is used to add diffusion in the propagation of the magnetic field as described in the model section. The ionospheric obstacle is approximated as a superconducting sphere and, thus, not allowing any diffusion of the magnetic field in the ionosphere. However, allowing a finite resistivity within the obstacle, or other structured (e.g. layered) resistivity profiles, could be implemented to investigate cases when the ionospheres of unmagnetized planets become magnetized, for example, under enhanced dynamic pressure of the solar wind [Luhmann *et al.*, 1980]. Further, 3-dimensional resistivity profiles have been used to study the surface conductivity of a terrestrial planet in a global hybrid model [Janhunen and Kallio, 2004].

Run 2 was used in the detailed analysis of ion spectra and energization. Difference between the two performed simulation runs is the upstream IMF components and the solar wind density (Table 1). The structure of the Mars induced magnetosphere is quite similar between the two runs as the IMF cone angle and magnitude is almost the same. The IMF clock angle differs by 48° between the runs. This means that the induced magnetosphere rotated in the direction perpendicular to incident solar wind flow between the MAVEN inbound and outbound bow shock crossings. The effects of IMF rotations on the Mars plasma environment can be studied in global models [Modolo *et al.*, 2012]. However, to implement such rotations accurately, magnetic field measurements are needed from the

upstream of the bow shock in the same time when another spacecraft is sampling the induced magnetosphere. The solar wind density changes by 25% between the two runs, which can lead to the bow shock moving closer to the planet and the more compressed induced magnetosphere in Run 2 compared to Run 1.

The simulation runs analyzed here use the exospheric neutral profiles defined in the ISSI model challenge for comparative global modeling studies [Brain *et al.*, 2010; Kallio *et al.*, 2010; Modolo *et al.*, 2016]. The upstream conditions and the ionospheric emission rates were chosen specifically to this case study, which is the the first attempt to compare multi-spacecraft observations from the Mars plasma environment to a global hybrid simulation. The role of the upper atmospheric variability over different time scales on the Mars plasma environment and atmospheric escape should be further studied in global models in light of new observations [Krasnopolsky, 2002; Chaffin *et al.*, 2014; Bougher *et al.*, 2015; Bhattacharyya *et al.*, 2015; Halekas, 2017].

5.2. Escape rates

The global escape rates from Mars (\mathcal{E}) in the analyzed simulation Run 2 are the following (with the escape rate divided by the injection rate in parentheses): $\mathcal{E}(\text{O}^+) = 1.7 \times 10^{25} \text{ s}^{-1}$ (38%), $\mathcal{E}(\text{O}_2^+) = 2.1 \times 10^{25} \text{ s}^{-1}$ (35%) and $\mathcal{E}(\text{H}^+) = 3.6 \times 10^{24} \text{ s}^{-1}$ (98%). The rates were determined by subtracting the rate of ions impacting the inner boundary from the injection rate. Note that only the photoionization of the Martian exosphere is considered explicitly in this study as the focus is on the heavy ion energization in the induced magnetosphere. Other ionization processes affect both the rate and spatial distribution of planetary ion production at Mars. The escape rates are listed here for completeness.

6. Summary

We studied oxygen ion energization in the Mars-solar wind interaction by comparing particle and magnetic field observations on the Mars Express and MAVEN missions to a global hybrid simulation. We found that large-scale structures of the Martian induced magnetosphere and plasma environment as well as the Mars heavy ion plume as seen by multi-spacecraft observations are reproduced by the model. Using the simulation we estimated the dynamics of escaping oxygen ions by analyzing their distance and time of flight as a function of the gained kinetic energy along spacecraft trajectories. In the upstream region the heavy ion energization resembles single particle solar wind ion pickup acceleration as expected, while within the induced magnetosphere the energization displays other features including the heavy ion plume from the ionosphere. Oxygen ions take up to 80 s and travel the distance of 20 000 km after their emission from the ionosphere toward the induced magnetosphere or photoionization from the neutral exosphere before they have reached energies of 10 keV in the plume along the analyzed spacecraft orbits. Lower oxygen ion energies of 100 eV are reached faster in 10-20 s over the distance of 100-200 km in the plume. Our finding suggests that oxygen ions are typically observed within the first half of their gyro phase if the spacecraft periapsis is on the hemisphere where the solar wind convection electric field points away from Mars.

Acknowledgments. The work of the lead author including the development of the RHybrid simulation platform was carried out during his Academy of Finland Postdoctoral Researcher project (Decision No. 257831). The work of MAVEN's SWIA, STATIC and magnetometer and MEX/ASPERA-3 instrument teams are acknowledged for providing high quality observations. Figures 1d-f were created using the VisIt open source

visualization tool [Childs et al., 2012]. Panels a, c, e and g of Figure 3 were created with the AMDA science analysis system (<http://amda.cdpp.eu/>) provided by the Centre de Données de la Physique des Plasmas (CDPP) supported by CNRS, CNES, Observatoire de Paris and Université Paul Sabatier, Toulouse. Global hybrid simulations were performed using the RHybrid simulation platform, which is available under an open source license by the Finnish Meteorological Institute (<https://github.com/fmihpc/rhybrid>). The simulation data that support the findings of this study are available from the corresponding author upon reasonable request. MAVEN and Mars Express data are openly available on the NASA's Planetary Data System (<https://pds.nasa.gov/>) and the ESA's Planetary Science Archive (<https://www.cosmos.esa.int/web/psa>).

References

- Barabash, S., and R. Lundin (2006), ASPERA-3 on Mars Express, *182*, 301–307, doi:10.1016/j.icarus.2006.02.015.
- Barabash, S., A. Fedorov, R. Lundin, and J.-A. Sauvaud (2007), Martian Atmospheric Erosion Rates, *Science*, *315*, 501–, doi:10.1126/science.1134358.
- Bhattacharyya, D., J. T. Clarke, J.-L. Bertaux, J.-Y. Chaufray, and M. Mayyasi (2015), A strong seasonal dependence in the Martian hydrogen exosphere, *Geophys. Res. Lett.*, *42*, 8678–8685, doi:10.1002/2015GL065804.
- Boman, E. G., U. V. Catalyurek, C. Chevalier, and K. D. Devine (2012), The Zoltan and Isorropia parallel toolkits for combinatorial scientific computing: Partitioning, ordering, and coloring, *Scientific Programming*, *20*(2), 129–150.

Bougher, S. W., D. Pawlowski, J. M. Bell, S. Nelli, T. McDunn, J. R. Murphy, M. Chizek, and A. Ridley (2015), Mars Global Ionosphere-Thermosphere Model: Solar cycle, seasonal, and diurnal variations of the Mars upper atmosphere, *J. Geophys. Res.*, *120*, 311–342, doi:10.1002/2014JE004715.

Brain, D., S. Barabash, A. Boeswetter, S. Bougher, S. Brecht, G. Chanteur, D. Hurley, E. Dubinin, X. Fang, M. Fraenz, J. Halekas, E. Harnett, M. Holmstrom, E. Kallio, H. Lammer, S. Ledvina, M. Liemohn, K. Liu, J. Luhmann, Y. Ma, R. Modolo, A. Nagy, U. Motschmann, H. Nilsson, H. Shinagawa, S. Simon, and N. Terada (2010), A comparison of global models for the solar wind interaction with Mars, *Icarus*, *206*, 139–151, doi:10.1016/j.icarus.2009.06.030.

Brain, D. A., J. P. McFadden, J. S. Halekas, J. E. P. Connerney, S. W. Bougher, S. Curry, C. F. Dong, Y. Dong, F. Eparvier, X. Fang, K. Fortier, T. Hara, Y. Harada, B. M. Jakosky, R. J. Lillis, R. Livi, J. G. Luhmann, Y. Ma, R. Modolo, and K. Seki (2015), The spatial distribution of planetary ion fluxes near Mars observed by MAVEN, *Geophys. Res. Lett.*, *42*, 9142–9148, doi:10.1002/2015GL065293.

Brecht, S. H. (1990), Magnetic asymmetries of unmagnetized planets, *Geophys. Res. Lett.*, *17*, 1243–1246, doi:10.1029/GL017i009p01243.

Chaffin, M. S., J.-Y. Chaufray, I. Stewart, F. Montmessin, N. M. Schneider, and J.-L. Bertaux (2014), Unexpected variability of Martian hydrogen escape, *Geophys. Res. Lett.*, *41*, 314–320, doi:10.1002/2013GL058578.

Childs, H., E. Brugger, B. Whitlock, J. Meredith, S. Ahern, D. Pugmire, K. Biagas, M. Miller, C. Harrison, G. H. Weber, H. Krishnan, T. Fogal, A. Sanderson, C. Garth, E. W. Bethel, D. Camp, O. Rübél, M. Durant, J. M. Favre, and P. Navrátil (2012),

VisIt: An End-User Tool For Visualizing and Analyzing Very Large Data, in *High Performance Visualization—Enabling Extreme-Scale Scientific Insight*, pp. 357–372.

Connerney, J. E. P., J. Espley, P. Lawton, S. Murphy, J. Odom, R. Oliverson, and D. Sheppard (2015), The MAVEN Magnetic Field Investigation, *Space Sci. Rev.*, *195*, 257–291, doi:10.1007/s11214-015-0169-4.

Curry, S. M., J. G. Luhmann, Y. J. Ma, C. F. Dong, D. Brain, F. Leblanc, R. Modolo, Y. Dong, J. McFadden, J. Halekas, J. Connerney, J. Espley, T. Hara, Y. Harada, C. Lee, X. Fang, and B. Jakosky (2015a), Response of Mars O⁺ pickup ions to the 8 March 2015 ICME: Inferences from MAVEN data-based models, *Geophys. Res. Lett.*, *42*, 9095–9102, doi:10.1002/2015GL065304.

Curry, S. M., J. Luhmann, Y. Ma, M. Liemohn, C. Dong, and T. Hara (2015b), Comparative pick-up ion distributions at Mars and Venus: Consequences for atmospheric deposition and escape, *Planet. Space Sci.*, *115*, 35–47, doi:10.1016/j.pss.2015.03.026.

Dai, W., and P. R. Woodward (1998), On the Divergence-free Condition and Conservation Laws in Numerical Simulations for Supersonic Magnetohydrodynamic Flows, *ApJ*, *494*, 317, doi:10.1086/305176.

Dong, Y., X. Fang, D. A. Brain, J. P. McFadden, J. S. Halekas, J. E. Connerney, S. M. Curry, Y. Harada, J. G. Luhmann, and B. M. Jakosky (2015), Strong plume fluxes at Mars observed by MAVEN: An important planetary ion escape channel, *Geophys. Res. Lett.*, *42*, 8942–8950, doi:10.1002/2015GL065346.

Dubinin, E., G. Chanteur, M. Fraenz, R. Modolo, J. Woch, E. Roussos, S. Barabash, R. Lundin, and J. D. Winningham (2008), Asymmetry of plasma fluxes at Mars. ASPERA-3 observations and hybrid simulations, *Planet. Space Sci.*, *56*, 832–835, doi:

10.1016/j.pss.2007.12.006.

Fedorov, A., E. Budnik, J.-A. Sauvaud, C. Mazelle, S. Barabash, R. Lundin, M. Acuña, M. Holmström, A. Grigoriev, M. Yamauchi, H. Andersson, J.-J. Thocaven, D. Winningham, R. Frahm, J. R. Sharber, J. Scherrer, A. J. Coates, D. R. Linder, D. O. Kataria, E. Kallio, H. Koskinen, T. Säles, P. Riihelä, W. Schmidt, J. Kozyra, J. Luhmann, E. Roelof, D. Williams, S. Livi, C. C. Curtis, K. C. Hsieh, B. R. Sandel, M. Grande, M. Carter, S. McKenna-Lawler, S. Orsini, R. Cerulli-Irelli, M. Maggi, P. Wurz, P. Bochsler, N. Krupp, J. Woch, M. Fränz, K. Asamura, and C. Dierker (2006), Structure of the martian wake, *182*, 329–336, doi:10.1016/j.icarus.2005.09.021.

Halekas, J. S. (2017), Seasonal variability of the hydrogen exosphere of Mars, *J. Geophys. Res.*, *122*, 901–911, doi:10.1002/2017JE005306.

Halekas, J. S., E. R. Taylor, G. Dalton, G. Johnson, D. W. Curtis, J. P. McFadden, D. L. Mitchell, R. P. Lin, and B. M. Jakosky (2015), The Solar Wind Ion Analyzer for MAVEN, *Space Sci. Rev.*, *195*, 125–151, doi:10.1007/s11214-013-0029-z.

Hara, T., K. Seki, Y. Futaana, M. Yamauchi, S. Barabash, A. O. Fedorov, M. Yagi, and D. C. Delcourt (2013), Statistical properties of planetary heavy-ion precipitations toward the Martian ionosphere obtained from Mars Express, *J. Geophys. Res.*, *118*, 5348–5357, doi:10.1002/jgra.50494.

Hietala, H., A. Sandroos, and R. Vainio (2012), Particle Acceleration in Shock-Shock Interaction: Model to Data Comparison, *The Astrophysical Journal Letters*, *751*, L14, doi:10.1088/2041-8205/751/1/L14.

Jakosky, B. M., J. M. Grebowsky, J. G. Luhmann, J. Connerney, F. Eparvier, R. Ergun, J. Halekas, D. Larson, P. Mahaffy, J. McFadden, D. F. Mitchell, N. Schneider, R. Zurek,

S. Bougher, D. Brain, Y. J. Ma, C. Mazelle, L. Andersson, D. Andrews, D. Baird, D. Baker, J. M. Bell, M. Benna, M. Chaffin, P. Chamberlin, Y.-Y. Chaufray, J. Clarke, G. Collinson, M. Combi, F. Crary, T. Cravens, M. Crismani, S. Curry, D. Curtis, J. Deighan, G. Delory, R. Dewey, G. DiBraccio, C. Dong, Y. Dong, P. Dunn, M. Elrod, S. England, A. Eriksson, J. Espley, S. Evans, X. Fang, M. Fillingim, K. Fortier, C. M. Fowler, J. Fox, H. Gröller, S. Guzewich, T. Hara, Y. Harada, G. Holsclaw, S. K. Jain, R. Jolitz, F. Leblanc, C. O. Lee, Y. Lee, F. Lefevre, R. Lillis, R. Livi, D. Lo, M. Mayyasi, W. McClintock, T. McEnulty, R. Modolo, F. Montmessin, M. Morooka, A. Nagy, K. Olsen, W. Peterson, A. Rahmati, S. Ruhunusiri, C. T. Russell, S. Sakai, J.-A. Sauvaud, K. Seki, M. Steckiewicz, M. Stevens, A. I. F. Stewart, A. Stiepen, S. Stone, V. Tennishev, E. Thiemann, R. Tolson, D. Toubanc, M. Vogt, T. Weber, P. Withers, T. Woods, and R. Yelle (2015), MAVEN observations of the response of Mars to an interplanetary coronal mass ejection, *Science*, *350*, 0210, doi:10.1126/science.aad0210.

Janhunen, P., and E. Kallio (2004), Surface conductivity of Mercury provides current closure and may affect magnetospheric symmetry, *Ann. Geophys.*, *22*, 1829–1837.

Jarvinen, R., and E. Kallio (2014), Energization of planetary pickup ions in the solar system, *J. Geophys. Res.*, *119*, 219–236, doi:10.1002/2013JE004534.

Jarvinen, R., and A. Sandroos (2013), Solar wind interaction with Venus and Mars in a parallel hybrid code, in *EGU General Assembly Conference Abstracts, EGU General Assembly Conference Abstracts*, vol. 15, pp. EGU2013–4352.

Jarvinen, R., E. Kallio, P. Janhunen, S. Barabash, T. L. Zhang, V. Pohjola, and I. Silanpää (2009), Oxygen ion escape from Venus in a global hybrid simulation: role of the ionospheric O⁺ ions, *Ann. Geophys.*, *27*, 4333–4348.

Jarvinen, R., D. A. Brain, and J. G. Luhmann (2016), Dynamics of planetary ions in the induced magnetospheres of Venus and Mars, *Planet. Space Sci.*, *127*, 1–14, doi:10.1016/j.pss.2015.08.012.

Kallio, E. (2001), Escaping of planetary ions from Mars and Venus, *Adv. Space Res.*, *27*, 1815–1824, doi:10.1016/S0273-1177(01)00330-1.

Kallio, E., and P. Janhunen (2003), Modelling the solar wind interaction with Mercury by a quasi-neutral hybrid model, *Ann. Geophys.*, *21*, 2133–2145.

Kallio, E., R. Jarvinen, and P. Janhunen (2006), Venus solar wind interaction: Asymmetries and the escape of O⁺ ions, *Planet. Space Sci.*, *54*, 1472–1481, doi:10.1016/j.pss.2006.04.030.

Kallio, E., K. Liu, R. Jarvinen, V. Pohjola, and P. Janhunen (2010), Oxygen ion escape at Mars in a hybrid model: High energy and low energy ions, *Icarus*, *206*, 152–163, doi:10.1016/j.icarus.2009.05.015.

Koskinen, H. E. J. (2011), *Physics of Space Storms: From the Solar Surface to the Earth*, Springer-Verlag, ISBN:978-3-642-00310-3.

Krasnopolsky, V. A. (2002), Mars' upper atmosphere and ionosphere at low, medium, and high solar activities: Implications for evolution of water, *J. Geophys. Res.*, *107*, 5128, doi:10.1029/2001JE001809.

Leblanc, F., R. Modolo, S. Curry, J. Luhmann, R. Lillis, J. Y. Chaufray, T. Hara, J. McFadden, J. Halekas, F. Eparvier, D. Larson, J. Connerney, and B. Jakosky (2015), Mars heavy ion precipitating flux as measured by Mars Atmosphere and Volatile Evolution, *Geophys. Res. Lett.*, *42*, 9135–9141, doi:10.1002/2015GL066170.

Ledvina, S. A., S. H. Brecht, D. A. Brain, and B. M. Jakosky (2017), Ion escape rates from Mars: Results from hybrid simulations compared to MAVEN observations, *J. Geophys. Res.*, *122*, 8391–8408, doi:10.1002/2016JA023521.

Luhmann, J. G., R. C. Elphic, C. T. Russell, J. D. Mihalov, and J. H. Wolfe (1980), Observations of large scale steady magnetic fields in the dayside Venus ionosphere, *Geophys. Res. Lett.*, *7*, 917–920, doi:10.1029/GL007i011p00917.

Luhmann, J. G., R. E. Johnson, and M. H. G. Zhang (1992), Evolutionary impact of sputtering of the Martian atmosphere by O(+) pickup ions, *Geophys. Res. Lett.*, *19*, 2151–2154, doi:10.1029/92GL02485.

Lundin, R. (2011), Ion Acceleration and Outflow from Mars and Venus: An Overview, *Space Sci. Rev.*, *162*, 309–334, doi:10.1007/s11214-011-9811-y.

Ma, Y. J., C. T. Russell, X. Fang, Y. Dong, A. F. Nagy, G. Toth, J. S. Halekas, J. E. P. Connerney, J. R. Espley, P. R. Mahaffy, M. Benna, J. P. McFadden, D. L. Mitchell, and B. M. Jakosky (2015), MHD model results of solar wind interaction with Mars and comparison with MAVEN plasma observations, *Geophys. Res. Lett.*, *42*, 9113–9120, doi:10.1002/2015GL065218.

Matsunaga, K., K. Seki, D. A. Brain, T. Hara, K. Masunaga, J. P. Mcfadden, J. S. Halekas, D. L. Mitchell, C. Mazelle, J. R. Espley, J. Gruesbeck, and B. M. Jakosky (2017), Statistical Study of Relations Between the Induced Magnetosphere, Ion Composition, and Pressure Balance Boundaries Around Mars Based On MAVEN Observations, *J. Geophys. Res.*, *122*, 9723–9737, doi:10.1002/2017JA024217.

McFadden, J. P., O. Kortmann, D. Curtis, G. Dalton, G. Johnson, R. Abiad, R. Sterling, K. Hatch, P. Berg, C. Tiu, D. Gordon, S. Heavner, M. Robinson, M. Marckwordt,

- R. Lin, and B. Jakosky (2015), MAVEN SupraThermal and Thermal Ion Composition (STATIC) Instrument, *Space Sci. Rev.*, *195*, 199–256, doi:10.1007/s11214-015-0175-6.
- Modolo, R., G. M. Chanteur, and E. Dubinin (2012), Dynamic Martian magnetosphere: Transient twist induced by a rotation of the IMF, *Geophys. Res. Lett.*, *39*, L01106, doi:10.1029/2011GL049895.
- Modolo, R., S. Hess, M. Mancini, F. Leblanc, J.-Y. Chaufray, D. Brain, L. Leclercq, R. Esteban-Hernández, G. Chanteur, P. Weill, F. González-Galindo, F. Forget, M. Yagi, and C. Mazelle (2016), Mars-solar wind interaction: LatHyS, an improved parallel 3-D multispecies hybrid model, *J. Geophys. Res.*, *121*, 6378–6399, doi:10.1002/2015JA022324.
- Najib, D., A. F. Nagy, G. Tóth, and Y. Ma (2011), Three-dimensional, multifluid, high spatial resolution MHD model studies of the solar wind interaction with Mars, *J. Geophys. Res.*, *116*, A05204, doi:10.1029/2010JA016272.
- Nilsson, H., N. J. T. Edberg, G. Stenberg, S. Barabash, M. Holmström, Y. Futana, R. Lundin, and A. Fedorov (2011), Heavy ion escape from Mars, influence from solar wind conditions and crustal magnetic fields, *Icarus*, *215*, 475–484, doi:10.1016/j.icarus.2011.08.003.
- Pohjola, V., and E. Kallio (2010), On the modeling of planetary plasma environments by a fully kinetic electromagnetic global model HYB-em, *Ann. Geophys.*, *28*, 743–751, doi:10.5194/angeo-28-743-2010.
- Sandroos, A. (2013), CORSAIR Solar Energetic Particle Model, in *American Geophysical Union, Spring Meeting 2013*, AGU Spring Meeting Abstracts, pp. SH53B–01.

Shimazu, H. (1999), Three-dimensional hybrid simulation of magnetized plasma flow around an obstacle, *Earth Planets Space*, 51, 383–393.

Accepted Article

Table 1. Simulation configuration and upstream solar wind (SW) and interplanetary magnetic field (IMF) conditions. Run 1 uses the conditions determined at the MAVEN inbound (ib) bow shock crossing and Run 2 uses the conditions determined at the MAVEN outbound (ob) and MEX inbound bow shock crossing. The cone angle is defined as $\arctan(\sqrt{B_y^2 + B_z^2}, B_x)$ and the clock angle is defined as $\arctan(B_y, B_z)$.

Parameter	Value
Box size ($x \times y \times z$) [R_M]	$(-4...4) \times (-4...4) \times (-4...4)$
Number of grid cells ($n_x \times n_y \times n_z$)	$240 \times 240 \times 240$
Grid cell size (Δx^3)	$(R_M/30)^3 = (113 \text{ km})^3$
Avg. macroparticles per cell	85
Timestep (Δt)	7.5 ms
Solution snapshot time	600 s
SW velocity [V_x, V_y, V_z]	$[-300, 0, 0] \text{ km s}^{-1}$
SW ion temperature	60 000 K
Run 1 (MAVEN ib)	
IMF [B_x, B_y, B_z]	$[3.5, 5.3, -0.8] \text{ nT}$
IMF magnitude	6.4 nT
IMF cone angle	57°
IMF clock angle	98°
SW ion density [cm^{-3}]	$n(\text{H}^+) = 15, n(\text{He}^{++}) = 0.75$
Run 2 (MAVEN ob and MEX ib)	
IMF [B_x, B_y, B_z]	$[4.3, 4.0, 3.3] \text{ nT}$
IMF magnitude	6.7 nT
IMF cone angle	51°
IMF clock angle	50°
SW ion density [cm^{-3}]	$n(\text{H}^+) = 20, n(\text{He}^{++}) = 1.0$
O^+ ionospheric emission rate	$4.2 \times 10^{25} \text{ s}^{-1}$
O_2^+ ionospheric emission rate	$6.0 \times 10^{25} \text{ s}^{-1}$
O^+ exospheric production rate	$1.57 \times 10^{24} \text{ s}^{-1}$
H^+ exospheric production rate	$3.64 \times 10^{24} \text{ s}^{-1}$
Ionospheric emis. radius	$R_v + 400 \text{ km}$
Zero resistivity (obstacle) radius	$R_v + 300 \text{ km}$
Particle absorption radius	$R_v + 200 \text{ km}$

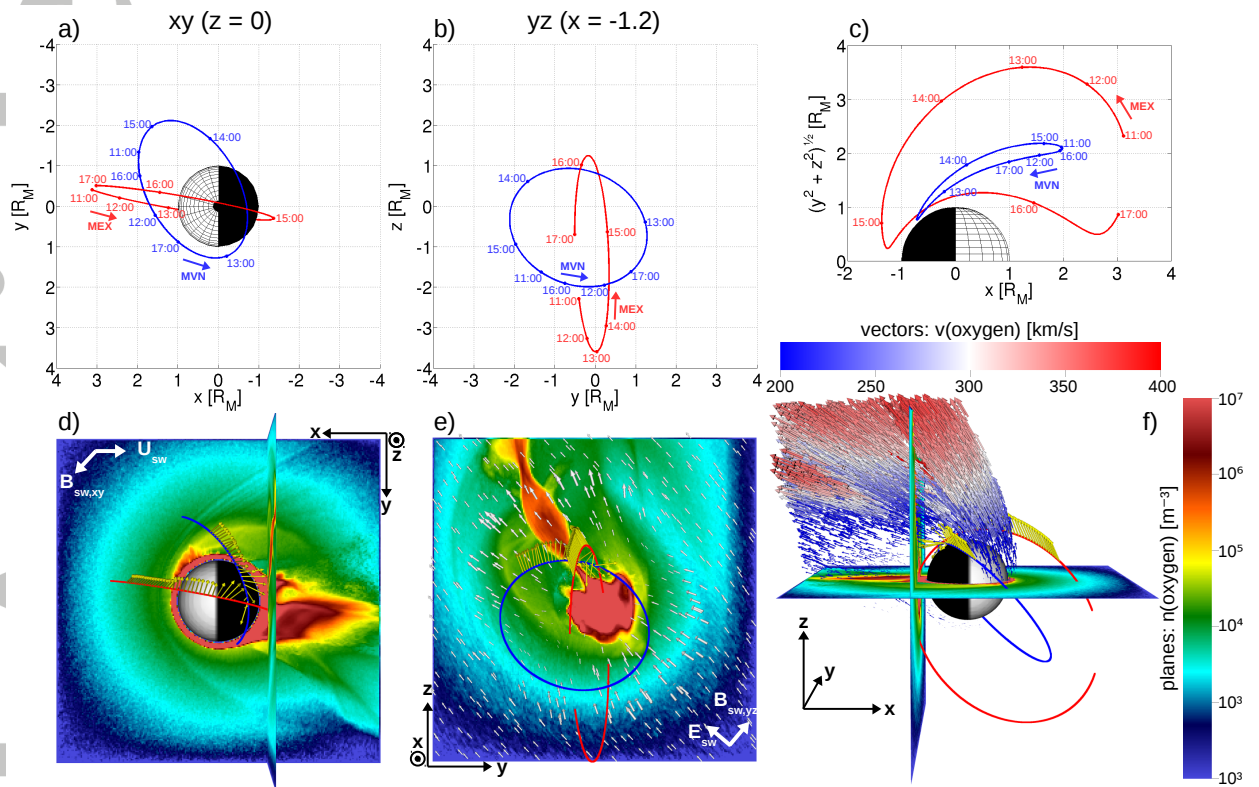


Figure 1. (top) Mars Express (red line) and MAVEN (blue line) orbits on Jan 25, 2015 analyzed in this study. (bottom) Escaping oxygen ions (ionospheric O^+ and O_2^+ ions and exospheric O^+ photoions) from Mars in the simulation Run 2. Colored surfaces give Martian oxygen ion density at $z = 0$ and $x = -1.2 R_M$ planes. (d-f) Yellow arrows on the orbit curves are oxygen ion velocity unit vectors in the simulation in the region where the ion plume was observed by the spacecraft. (e) White arrows show the electric field at $x = -1.2 R_M$ plane. (f) Colored arrows display oxygen ion velocity vectors in the regions of highest oxygen ion flux ($nv > 10^{10} \text{ m}^{-2}\text{s}^{-1}$). (d-e) U_{sw} , B_{sw} and E_{sw} arrows display the orientation of the undisturbed upstream solar wind flow, magnetic field and electric field, respectively.

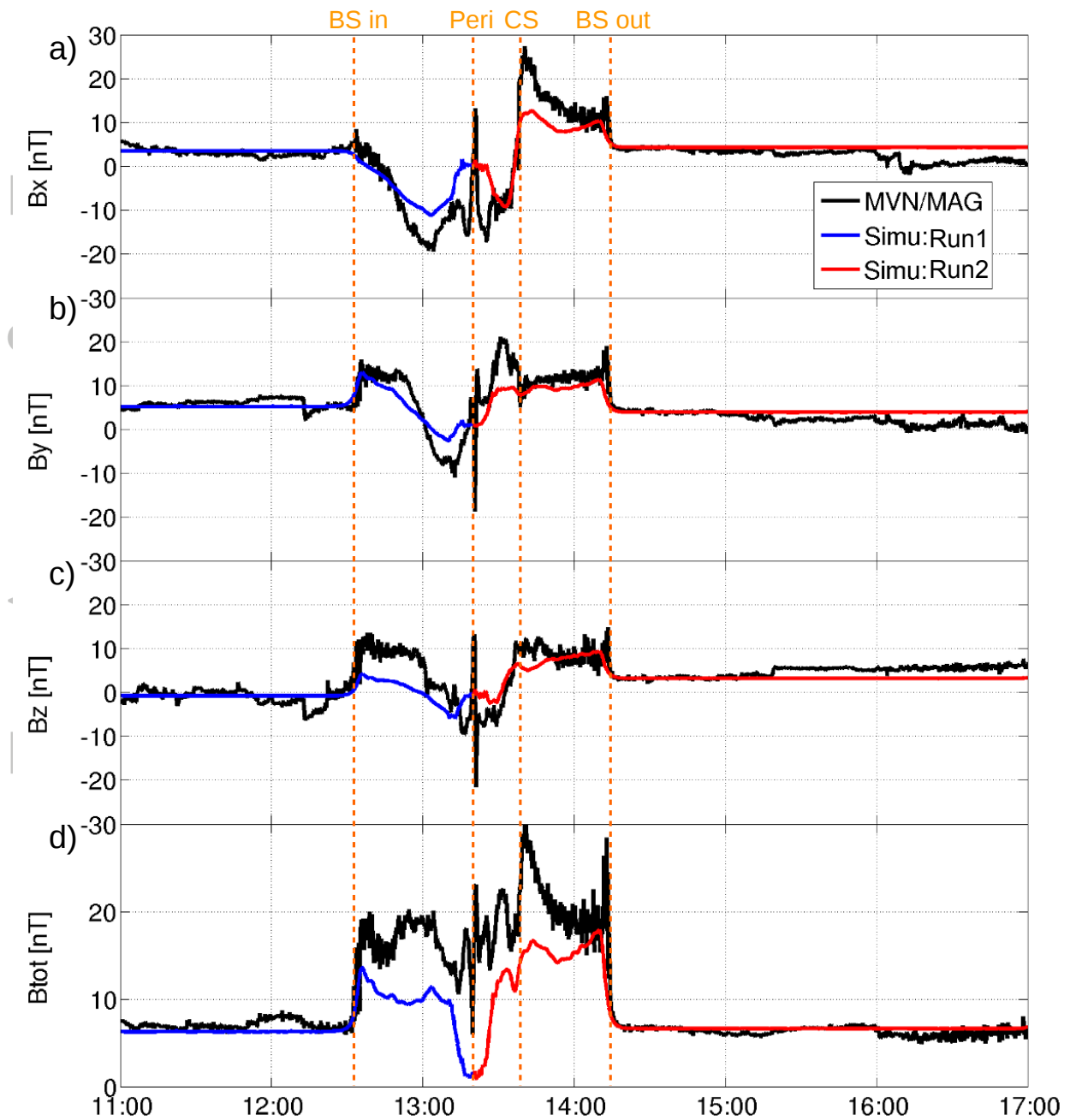


Figure 2. MAVEN magnetic field observations (black line) compared to the simulation Run 1 with inbound upstream conditions (blue line) and Run 2 with outbound conditions (red line). Orange vertical lines indicate the crossing of the inbound bow shock (BS in), the crossing of the outbound bow shock (BS out), the periapsis of MAVEN orbit (Peri) and the crossing of the central tail current sheet (CS).

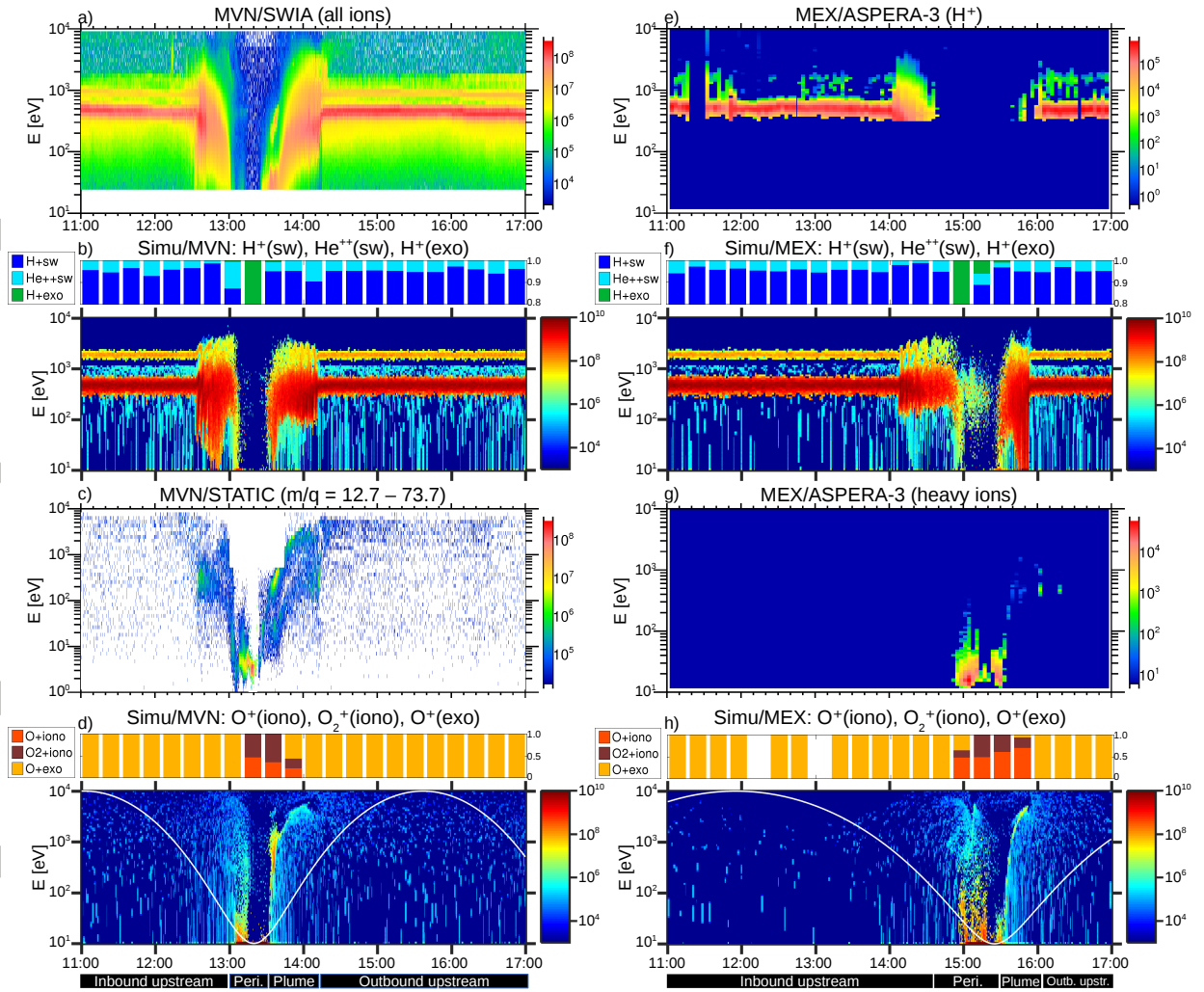


Figure 3. Ion time-energy spectrograms observed by MAVEN (left) and Mars Express (right) compared to the simulation Run 2. Observations show all MVN/SWIA ions, MVN/STATIC heavy ions, MEX/ASPERA-3/IMA protons and MEX/ASPERA-3/IMA heavy ions. The model spectra show omnidirectional differential ion flux gathered along the spacecraft trajectories with the coloring determined as $\sum_i w_i v_i / (4\pi \Delta V \Delta E)$ [$\# / (\text{s m}^2 \text{ eV sr})$], where the summation i is over macroions in a spatial cell (ΔV is the cell volume) and energy range $[E, E + \Delta E]$, w_i is the statistical weight of a macroion, v_i is the speed of a macroion and the full solid angle is used to normalize the flux. The MVN/SWIA and MVN/STATIC plots are in the units of differential ion energy flux [$\text{eV} / (\text{s cm}^2 \text{ eV sr})$], whereas MEX/ASPERA-3/IMA plots are in the units of differential ion energy flux [$\# / (\text{s cm}^2 \text{ eV sr})$]. Above the model spectra relative ion concentrations are shown for the solar wind protons and alphas ($\text{H}^+(\text{sw})$ and $\text{He}^{++}(\text{sw})$), exospheric photoionized protons ($\text{H}^+(\text{exo})$), atomic and molecular oxygen ions emitted from the ionosphere ($\text{O}^+(\text{iono})$ and $\text{O}_2^+(\text{iono})$) and exospheric photoionized atomic oxygen ions ($\text{O}^+(\text{exo})$). White curves in panels d and h show the evolution of the spacecraft altitude as a function of time for context. The linear altitude curves (the linear scale not shown) are fitted in the panels in such a way that the orbit apoapses coincide with the maximum value of the vertical axis and the orbit periapses coincide with the minimum value of the vertical axis (see the orbits in Figure 1). At the bottom are denoted the inbound upstream, periapsis, plume and outbound upstream intervals.

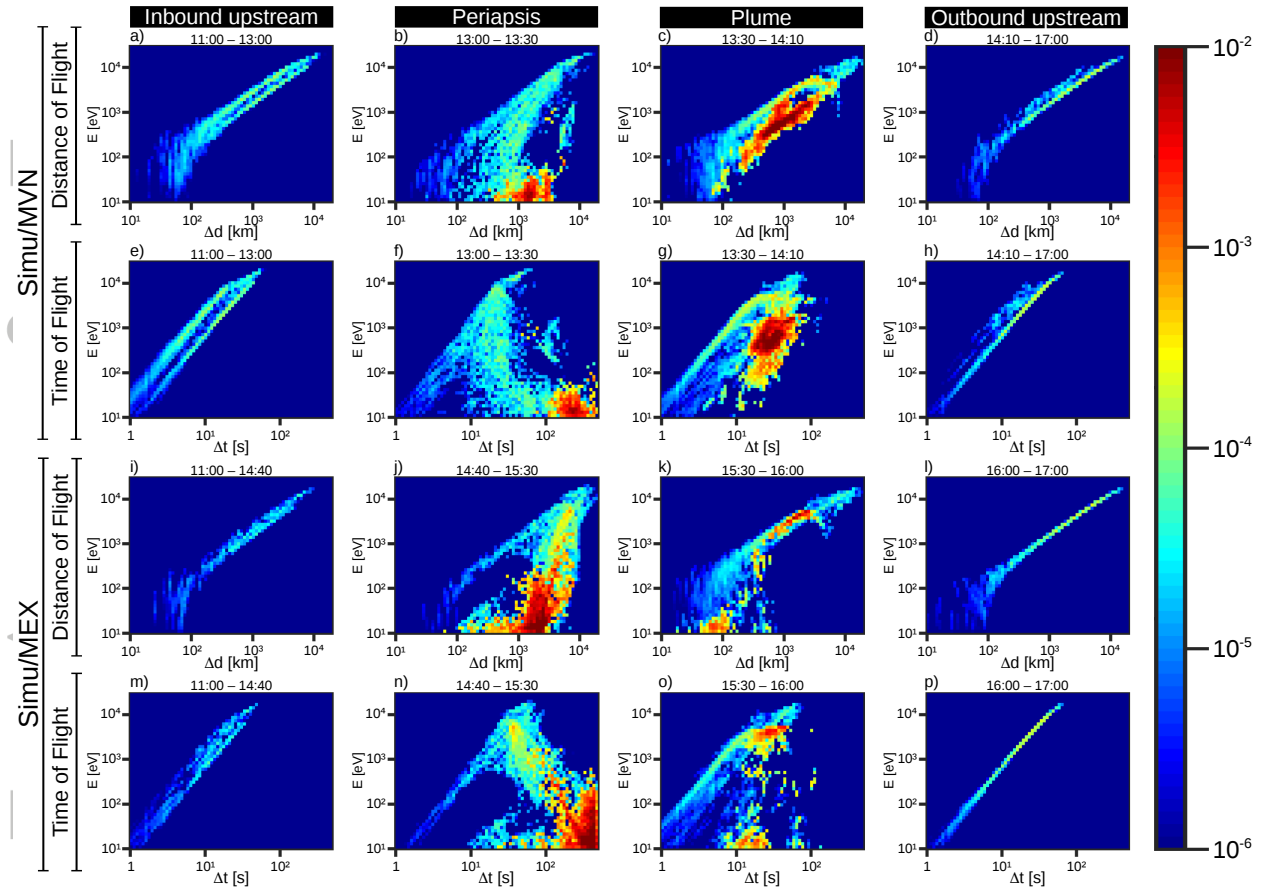


Figure 4. Probability density maps of the oxygen ion energy (E) as a function of the distance of flight ($\Delta d = \text{DoF}$) and the time of flight ($\Delta t = \text{ToF}$) along the spacecraft trajectories in the simulation Run 2. Ion counts at four time intervals (inbound upstream, periapsis, plume and outbound upstream) from panels d and h of Figure 3 are included in these maps. Δd is the distance between the observation point and the ionization point. Δt is the duration from the ionization time to the observation time. The color scale is determined as $\sum_i w_i / w_{\text{all}}$, where the summation i is over ions in spatial cells along the spacecraft orbit in the time interval and in phase space cells $(\Delta d, \Delta E)$ and $(\Delta t, \Delta E)$, w_i is the weight of an ion and w_{all} is the sum of all ion weights in the spectra.

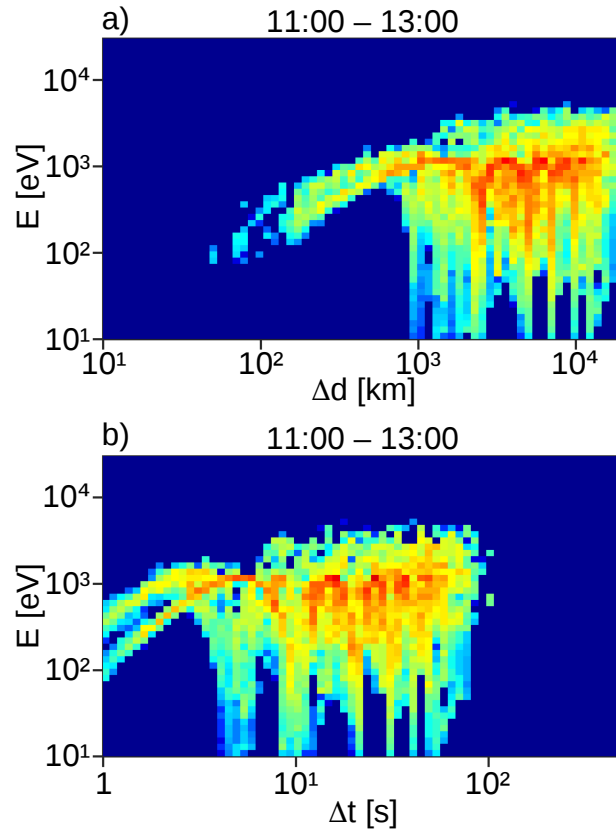


Figure 5. Probability density maps of the exospheric photoionized hydrogen ion energy (E) as a function of the distance of flight (Δd) and the time of flight (Δt) along the MAVEN trajectories in the simulation Run 2. Ion counts of $H^+(\text{exo})$ in Figure 3b are included in these maps. The figure is in the same format and color scale as panels a and e of Figure 4.